



Universiteit
Leiden
The Netherlands

Pixel super-resolution interference pattern sensing via the aliasing effect for laser frequency metrology

Wan, L.; Yu, T.; Zhao, d.; Löffler, W.

Citation

Wan, L., Yu, T., Zhao, D., & Löffler, W. (2023). Pixel super-resolution interference pattern sensing via the aliasing effect for laser frequency metrology. *Laser & Photonics Reviews*, 17(10). doi:10.1002/lpor.202200994

Version: Publisher's Version

License: [Creative Commons CC BY 4.0 license](https://creativecommons.org/licenses/by/4.0/)

Downloaded from: <https://hdl.handle.net/1887/3719366>

Note: To cite this publication please use the final published version (if applicable).

Pixel Super-Resolution Interference Pattern Sensing Via the Aliasing Effect for Laser Frequency Metrology

Lipeng Wan, Tianbao Yu, Daomu Zhao, and Wolfgang Löffler*

The superposition of several optical beams with large mutual angles results in sub-micrometer periodic patterns with a complex intensity, phase, and polarization structure. For high-resolution imaging thereof, one often employs optical super-resolution methods such as scanning nano-particle imaging. Here, it is reported that by using a conventional arrayed image sensor in combination with 2D Fourier analysis, the periodicities of light fields much smaller than the pixel size can be resolved in a simple and compact setup, with a resolution far beyond the Nyquist limit set by the pixel size. The ability to resolve periodicities with spatial frequencies of $\approx 3 \mu\text{m}^{-1}$, 15 times higher than the pixel sampling frequency of $0.188 \mu\text{m}^{-1}$, is demonstrated. This is possible by analyzing high-quality Fourier aliases in the first Brillouin zone. In order to obtain the absolute spatial frequencies of the interference patterns, simple rotation of the image sensor is sufficient, which modulates the effective pixel size and allows determination of the original Brillouin zone. Based on this method, wavelength sensing with a resolving power beyond 100,000 without any special equipment is demonstrated.

Also for the investigation of complex field configurations, periodic patterns need to be analyzed, such as for the recently discovered bright superchiral fields that can be synthesized by interference of several optical beams,^[2] and for exploration of more general interference phenomena.^[3] Several approaches have been reported for high-precision fringe metrology, using position sensing detectors,^[4] Fresnel zone plates,^[5] and heterodyne period measurements.^[6] Direct lens-free imaging of these fields is, however, considered to be impossible because of the large camera pixel size compared to the interference pattern periodicities, see **Figure 1**. The pixel size δ of modern charge-coupled device (CCD) or complementary metal-oxide-semiconductor (CMOS) image sensors is usually at least several micrometers due to limitations of the silicon base material and achievable signal-to-noise ratio,^[7]

1. Introduction

The precise measurement of periodicities of light fields, fringe metrology, is essential for various metrology tasks such as high-precision laser frequency determination, and angular and position sensing, which is for instance crucial in nanolithography.^[1]

resulting in a sampling frequency of $f_s = 1/\delta$. The Nyquist-Shannon sampling theorem^[8,9] tells us that only structures with spatial frequencies smaller than $f_s/2$ can be resolved in all detail, leading to the condition $f_s/2 > f_L$, where f_L is the spatial frequency of the interference pattern.


Known methods for probing optical fields on scales much smaller than usual pixel sizes include nanoparticle scanning methods^[10] near-field scanning optical microscopy (NSOM)^[11,12] and vectorial field reconstruction.^[13] The spatial resolution of these methods is ultimately limited by the size of the probe to ≈ 80 nm, and complex scanning equipment with nanometer precision is needed, and scanning-based methods are rather slow.

Here we report that periodic light structures can reliably be detected with a simple arrayed image sensor such as a CCD or CMOS camera by exploiting the aliasing effect happening for sampling below the Nyquist limit, sketched in **Figure 1**. We found that in 2D fast Fourier transforms of CMOS camera images, the “aliases” of the high-spatial-frequency interference patterns are clearly visible. Their spatial frequencies can be determined with remarkable precision, and also the relative phase of the beams can be retrieved with high accuracy. We show that the ambiguity of calculating the original spatial frequency from the measured spatial alias frequencies can be resolved by changing the effective image sensor pixel size simply by rotating the image sensor. This method is fast and the setup is extremely simple since it only employs an image sensor mounted on a rotation stage and no imaging optics. We demonstrate the measurement of interference

L. Wan, W. Löffler
Leiden Institute of Physics
Leiden University
Leiden, CA 2333, The Netherlands
E-mail: loeffler@physics.leidenuniv.nl

L. Wan, D. Zhao
Zhejiang Province Key Laboratory of Quantum Technology and Devices
School of Physics
Zhejiang University
Hangzhou 310027, China

L. Wan, T. Yu
School of Physics and Material Science
Nanchang University
Nanchang 330031, China

 The ORCID identification number(s) for the author(s) of this article can be found under <https://doi.org/10.1002/lpor.202200994>

© 2023 The Authors. Laser & Photonics Reviews published by Wiley-VCH GmbH. This is an open access article under the terms of the Creative Commons Attribution License, which permits use, distribution and reproduction in any medium, provided the original work is properly cited.

DOI: 10.1002/lpor.202200994

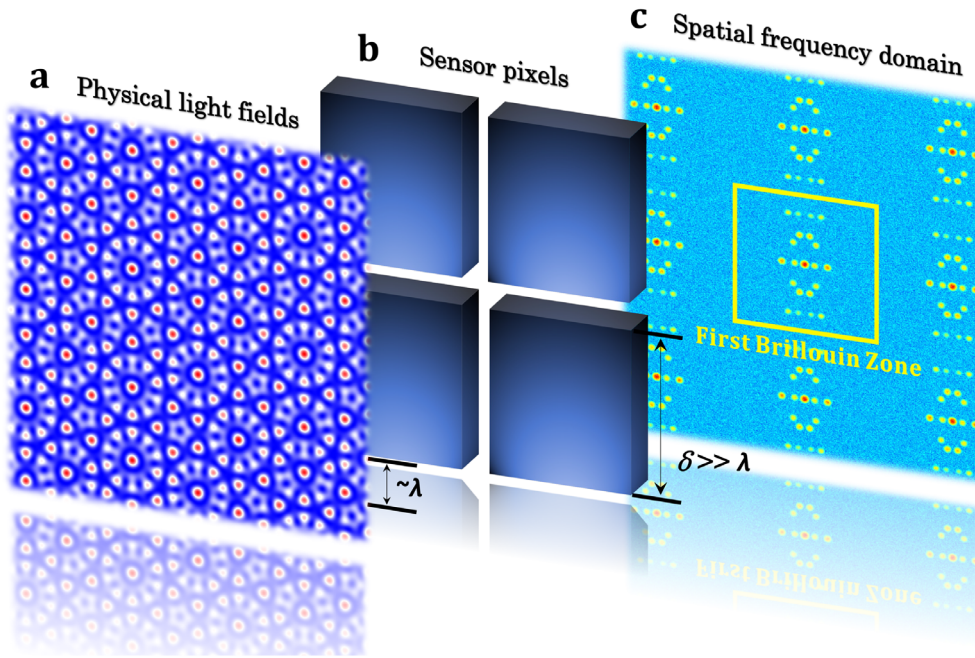


Figure 1. a) Illustration of mapping light fields b) using a standard image sensor whose pixel size is much larger than the periodicities of the interference pattern (a). c) In the Fourier transform of images captured by the camera, the aliases of high-spatial frequency components are clearly visible in the first Brillouin zone indicated by the yellow box.

periodicities 15 times smaller than the pixel size. Undersampling results in a reduction of the signal-to-noise ratio (SNR),^[14] but we find that this is not a major issue here and the dynamic range of standard CCD or CMOS detectors is sufficient. Undersampling is more often used in the temporal domain including in white-light interference microscopy as a function of path delay,^[15] but no study has directly been explored in the spatial domain with an arrayed image sensor, to our best knowledge.

We demonstrate a prototype of a high-precision wavemeter with a resolution of 5 μm using a 5.3 μm pixel-size image sensor. Reversely, if the laser wavelength is known, the same technique can be used to measure the angle between two laser beams with an accuracy of 8 μrad .

2. Theory and Arrangement

Plane-wave interference. Let us consider a superposition of N -plane electromagnetic waves with the same angular frequency $\omega = ck$ and a fixed phase relation. The resulting electric field is

$$\mathbf{E} = \text{Re } \tilde{\mathbf{E}} = \text{Re} \left(\sum_{j=1}^N \tilde{\mathbf{E}}_j e^{i(\mathbf{k}_j \cdot \mathbf{r} - \omega t)} \right). \quad (1)$$

Thus, the mean square of the electric field intensity is

$$S = \frac{1}{2} \tilde{\mathbf{E}} \cdot \tilde{\mathbf{E}}^* = \frac{1}{2} \left(\sum_{l=1}^N \tilde{\mathbf{E}}_l \cdot \tilde{\mathbf{E}}_l^* + \sum_{j=1}^N \sum_{l \neq j} \tilde{\mathbf{E}}_j \cdot \tilde{\mathbf{E}}_l^* e^{i(\mathbf{k}_j - \mathbf{k}_l) \cdot \mathbf{r}} \right), \quad (2)$$

where the first term is the zero-spatial-frequency background and the second term describes the pairwise interference resulting in

fringes that can be described by $\mathbf{k}_{jl} = \mathbf{k}_j - \mathbf{k}_l$ giving the orientation of the pattern with spatial frequency $f_{jl} = f_l = |\mathbf{k}_{jl}| / 2\pi$, assuming that the polarizations are not orthogonal, $\tilde{\mathbf{E}}_j \cdot \tilde{\mathbf{E}}_l^* \neq 0$.

By performing a continuous 2D Fourier transform of the mean square of the electric field, we obtain the corresponding field in the spatial-frequency domain

$$\tilde{S}(\mathbf{f}) = \alpha \delta(\mathbf{f}) + \sum_{j=1}^N \sum_{l \neq j} \gamma_{jl} \delta(\mathbf{k}_j - \mathbf{k}_l + 2\pi \mathbf{f}), \quad (3)$$

here, δ denotes the Dirac delta function, α is the zero-frequency intensity, and the weight functions $|\gamma_{jl}|$ and $\arg(\gamma_{jl})$ denote the magnitude and phase of the spatial frequency components. The vector \mathbf{f} describes the frequency and direction of the interference pattern from the plane-wave pair.

Image sensor sampling and Fourier transform. On an arrayed image sensor chip with a pixel pitch of δ_x and δ_y , the intensity is integrated over the area of each pixel in an incoherent way. The observation of such light fields with the image sensor $S_s(\mathbf{r})$ can be written as^[8]

$$S_s(\mathbf{r}) = [S(\mathbf{r}) \circledast S_p(\mathbf{r})] \cdot \Gamma(\mathbf{r}, \Delta \mathbf{r}). \quad (4)$$

Here the circled asterisk symbol stands for 2D convolution of the superposed light fields $S(\mathbf{r})$ with the pixel responsivity distribution $S_p(\mathbf{r})$, which is then filtered by a comb function Γ consisting of an array of Dirac delta functions characterized by the pixel spacing $\Delta \mathbf{r} = (\delta_x, \delta_y)$. Due to pixelation, the discrete Fourier transform of the light pattern sampled by the sensor array becomes (for a detailed derivation, see Supporting Information S1)

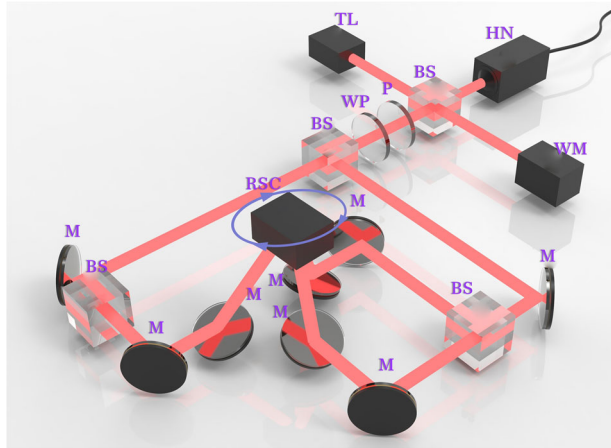


Figure 2. Experimental setup for pixel super-resolution interference pattern sensing: HN, He-Ne laser; TL, tunable laser diode NewFocus 6224; WM, wavemeter, HighFinesse WS6-200; RSC, rotating camera platform; M, mirror; BS, beam splitter; WP, half waveplate; P, polarizer.

$$\tilde{S}_s(f_x, f_y) = \sum_{u,v} \tilde{S}_p \left(f_x - \frac{u}{\delta_x}, f_y - \frac{v}{\delta_y} \right), \quad (5)$$

where the real integers u and v characterize the order of spatial aliasing and the complex function \tilde{S}_p gives the discrete response function

$$\tilde{S}_p(f_x, f_y) = \tilde{S}(f_x, f_y) \cdot \tilde{P}(f_x, f_y). \quad (6)$$

Here $\tilde{P}(f_x, f_y)$ is the Fourier transform of the two-dimensional pixel responsivity distribution within each pixel. For simplicity, we now assume that the image sensor has square pixels with $\delta_x = \delta_y = \delta = 1/f_s$. Equations (5) and (6) suggests that the nature of spatial sampling results in a periodic structure of the spatial frequency of the light fields, containing both the true spatial frequency $\tilde{S}_p(f_x, f_y)$ and its alias $\tilde{S}_p(f_x - uf_s, f_y - vf_s)$.^[8,16] Aliases appear if high spatial frequencies ($f > f_s/2$) “fold back” into the first Brillouin zone ($f < f_s/2$), a phenomenon analogous to the “Umklapp process” in solid-state physics. Thus, the real high spatial frequency of the light fields f_L at alias order n results in a different measured spatial frequency $f_m = |f_L - nf_s|$ for the 1D case and $\{f_x^m, f_y^m\} = \{|f_x - uf_s|, |f_y - vf_s|\}$ for the 2D case.

Resolving the frequency ambiguity.—In order to determine the original spatial frequency, one needs to determine the original Brillouin zone number. We found that by simply rotating the image sensor, the original Brillouin zone number can be determined and thus, the true spatial frequency of the light fields is determined. This is because the rotation of the image sensor around its center surface normally changes the effective image sensor pixel dimensions and thereby the sampling frequency f_s . From the perspective of the light field, its spatial frequencies f_{ji} are transformed into $f_{ji}^r(\theta) = \mathbf{R}_z(\theta) \cdot f_{ji}$, where $\mathbf{R}_z(\theta)$ is the standard rotation matrix – in Section 3 we discuss explicit cases.

Our experimental setup is shown in **Figure 2**. Although it is clear from Equation (5) that the pixel responsivity distribution of a specific image sensor is important, our method works for all types. Here we use a CMOS image sensor (Cinogy CMOS 1201-nano, i.e., a 5.3 μm pixel size image sensor without protective

glass) mounted at the center of a precision rotation stage Newport M-URM80APP controlled by a Newport ESP300 controller, with an angular resolution of 0.001°, allowing for continuous rotation of the sensor around its centered surface normal. In the process of retrieving the periodicities of the interference fringes of the superimposed light beams, all the necessary steps including rotation of the image sensor chip, recording of images, and performing fast 2D Fourier transforms (FFTs) are automated by a computer.

3. Measurements Results

3.1. One-Dimensional Interference Patterns

We consider first two-beam superpositions. For this configuration, the electric field vectors are chosen to be equal, $\tilde{\mathbf{E}}_{1,2} = [0, 1, 0]$ with respect to the image sensor plane, $\mathbf{k}_1 = k[\sin\psi, 0, \cos\psi]$ and $\mathbf{k}_2 = k[-\sin\psi, 0, \cos\psi]$ with $\psi = \pi/4$. From Equation (3) we determine that the spatial frequency of the interference pattern is 2234.85 mm^{-1} . The Nyquist frequency of our image sensor is 94.34 mm^{-1} , 23.7 times smaller. We record images while rotating the image sensor around its surface normally in steps of 0.1°. **Figure 3a** shows raw FFT images on a logarithmic scale, next to the strong zero-frequency peak, side peaks that are aliases of the high-spatial frequency interference patterns are clearly visible.

During rotation of the image sensor, we first determine the absolute frequency $f_m = |f_m|$, the result is shown in **Figure 3(b)**, together with numeric simulations. The pattern shows a periodicity of 90°, and mirror symmetry with symmetry axes at $45 + \ell \cdot 90^\circ$, $\ell \in \mathbb{Z}$, which originates from D_4 group of symmetry of the square shape of the pixel. We observe a good agreement between the experiment and simulation (see also Supporting Information S2).

To gain further insight, we perform the analysis over one cycle denoted by the orange box and analyze the x and y spatial frequency components, shown in **Figure 3c** for x -component and **3(d)** for the y -component. We observe an oscillation of the spatial frequency components upon rotation; a cycle is again completed after rotation over 90°. We now focus on the spatial frequency in x direction. At $\theta = 0$, the x -axis is aligned along the interference fringes, where the image sensor observes zero spatial frequency (which can hardly be determined experimentally because of the overlap with the zero-frequency background). If the sensor is rotated, the Fourier frequency increases until it reaches the Nyquist criterion, where it is folded back and further rotation results in a decrease in the measured (alias) spatial frequency; this process is repeated until the x -axis is perpendicular to the fringes ($\theta = 90$ degrees). Thus, the observed oscillation pattern is in effect a manifestation of folding, where the high spatial frequencies beyond the first Brillouin zone oscillate back and forth across the positive half of the first Brillouin zone upon rotation. From this physical picture, the x -component of the true spatial frequencies f_x^r upon rotation can be deduced to be (a detailed derivation is shown in Supporting Information S3)

$$f_x^r(\theta, f_{bz}, f_x^m) = \left(m + \frac{1}{2} - \frac{1}{2} \cos m\pi \right) f_{bz} + f_x^m(\theta) \cos m\pi, \quad (7)$$

where f_x^m is the measured x -component of the spatial frequency upon rotation. The y -frequency component f_y^r exhibits a reverse

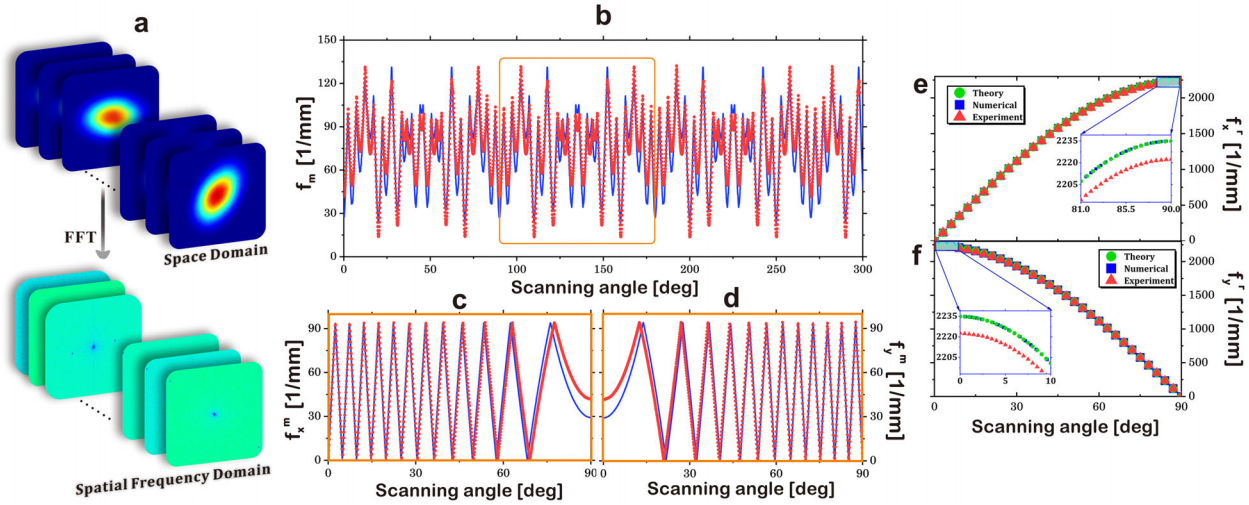


Figure 3. Probing superposed light fields using a CMOS image sensor with a $5.3 \mu\text{m}$ pixel pitch, where the structure of the interference pattern is much smaller than the pixel size. The image sensor is mounted on Newport M-URM80APP to form a custom-made rotating image sensor platform. a) For a continuous rotation shows examples of captured intensity images in the space domain and the corresponding Fourier transform. Tracing the frequencies of Fourier peak gives b) the measured trajectories of spatial frequencies; we compare numerical simulations (blue lines) to the experimental data (red dots). The orange box denotes one cycle. Within one cycle, we disentangle and extract the individual components of trajectories of spatial frequencies for the c) X-component and d) Y-component. From this, we calculate the real spatial frequencies of the interference patterns for the e) X-component and f) Y-component. The inset in (e) and (f) are magnifications of the spatial frequencies near the flat regions of the trajectories. The numerical and experimental data show good agreement.

trajectory compared to the x -frequency component, due to the symmetry, and is

$$f_y^r(\theta', f_{bz}, f_y^m) = \left(m + \frac{1}{2} - \frac{1}{2} \cos m\pi\right) f_{bz} + f_y^m(\theta') \cos m\pi, \quad (8)$$

where $\theta' = \pi/2 - \theta$.

Figure 3e,f present the original frequency trajectories of the physical light field retrieved using Equations (7) and (8), together with the corresponding theoretical prediction from projection. The image sensor rotation induces a change of the true spatial frequency projected along the axis, where the other frequency component disappears at the end of the rotation trajectory and thus, the true spatial frequency of the light field is retrieved. For the measurements of the x component, we retrieve the spatial frequency of physical light fields to be $2222.3759 \text{ mm}^{-1}$, in excellent agreement with the simulation and theory. The slight deviation in the true spatial frequency is attributed to the imperfect alignment of the light beams. This shows that we can simply measure the beam half angles with very high precision using our rotation technique, which is, in our case, 44.6811 degrees (the precision will be discussed later). Further, we observe that the retrieved spatial frequencies retrieved through the x - and y -frequency components are in practice not equal, with the latter being $2222.7448 \text{ mm}^{-1}$. We argue that a residual tilt of the image sensor, or a small (75 pm) asymmetry of the image sensor pixels, is responsible for this.

3.2. Probing Superposition of Multiple Coherent Beams of Light

To further demonstrate the power of our technique, we show that the proposed method works also for multibeam superpositions, generating rich periodic patterns.^[3,17] It is clear from Equation (2)

Table 1. Three-beam interference configuration.

j	k_j	$\tilde{\mathbf{E}}_j$
P	$[\sin\psi, 0, \cos\psi]$	$[-\cos\psi \cos\varphi, -\sin\varphi, \sin\psi \cos\varphi]$
Q	$[-\sin\psi, 0, \cos\psi]$	$[\cos\psi \cos\varphi, \sin\varphi, \sin\psi \cos\varphi]e^{i\alpha}$
R	$[0, \sin\psi, \cos\psi]$	$[\sin\varphi, -\cos\psi \cos\varphi, \sin\psi \cos\varphi]e^{i\gamma}$

that every beam-pair superposition $\tilde{\mathbf{E}}_j \cdot \tilde{\mathbf{E}}_i^*$ produces a pattern with high spatial frequency that contributes to the overall superposed light field distribution, we now explore the three waves configuration shown in Figure 2. The specific parameters of this superposition are listed in Table 1, where the mutual beam half-angle is $\psi = \pi/4$, the phase $\varphi = \pi/4$, α and γ are the relative phase of the waves. When rotating the image sensor, we observe three distinct Fourier peak trajectories, as expected. All these Fourier peaks are traced simultaneously during image sensor rotation, the frequency trajectories measured along the y -direction are shown in Figure 4a, where the zone denoted by the orange box reveals a repeating pattern which are shifted for different beam combinations, containing information about their relative angles between the beams. By using Equation (8) one can retrieve the true spatial frequencies, whose retrieved trajectories are shown in Figure 4b. The true spatial frequencies can then be extracted from the end of the trajectories, where interference of the PR, PQ, and QR beam combinations are, respectively, 1573 , 2227 , and 1577 mm^{-1} . The theoretical predictions for perfect alignment are 1580 , 2235 and 1580 mm^{-1} , the errors are thus 0.45% , 0.36% , and 0.19% which we attribute to a small misalignment of the beams. This indicates the high precision of our method, and that it is also applicable to multiple-beam superpositions.

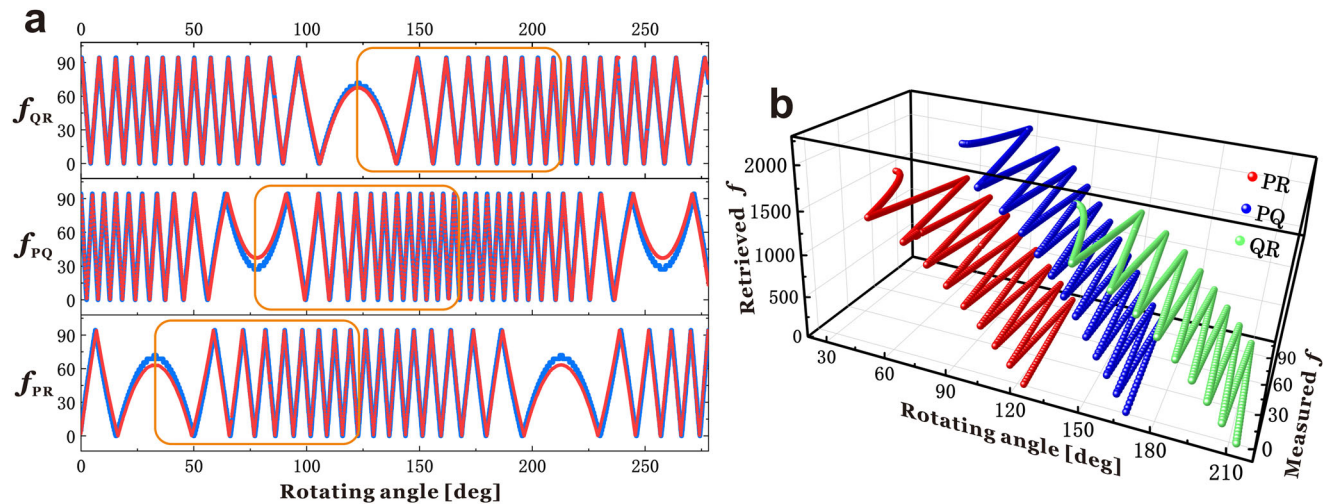


Figure 4. Resolving 3-beam light field superpositions. a) Rotation measurements in the under-sampled case showing numerical simulations (blue) and experimental measurements (red). The orange box shows the repeating pattern that is angle-shifted for different beam combinations. b) Retrieved spatial frequency trajectories for the 2D interference patterns. The spatial frequencies are shown in units of 1 mm^{-1} .

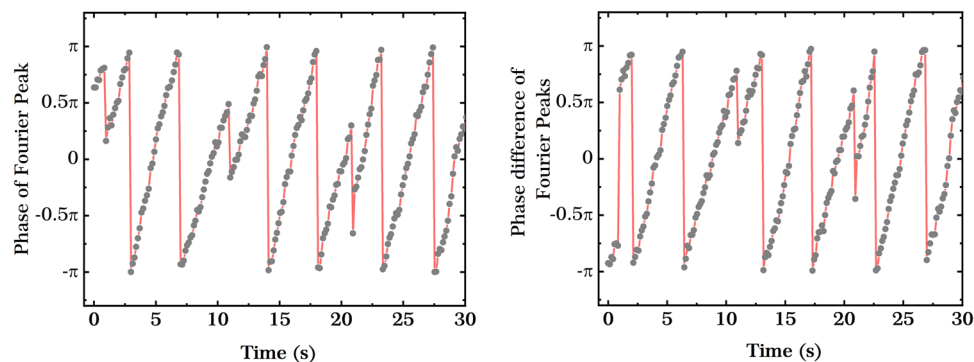


Figure 5. Demonstration of phase sensing. A sawtooth signal with a frequency of 100 mHz is imposed on the piezoelectric-actuated mirror. We measure the absolute Fourier peak phase (left) and the relative phase compared to another nonshifted beam combination (right).

4. Phase Retrieval

Having measured the spatial frequencies, we show that it is also possible to retrieve the relative phases of the beams in superposition using our method. From Equations (3)–(6) we see that the phase of the Fourier peak is independent of the pixel pitch as well as two-dimensional pixel responsivity distribution, i.e., the precise properties of sensor therefore play no role in the phase of the Fourier peak of the Fourier transform. Therefore, the relative-phase information of the superposed light beams can be obtained, even in the undersampled case.

To prove this point, we attach a piezo chip (Thorlabs PA4HEW) to one of the mirrors in one of the arms, this allows for finely tuning the path difference with nanoscale precision, inducing a shift of the fringes of the interference pattern. We apply to the piezo a sawtooth signal with a frequency of 100 mHz, **Figure 5a** shows the measured phase of the Fourier peak. We see that the Fourier phase changes mostly linearly with the applied voltage. Synchronously, we measure the relative phase change of this Fourier peak compared to another Fourier peak originating from two beams without a piezo element, shown in **Figure 5b**. We observe the same pattern except for a constant phase offset. This

proves our theoretical prediction, opening a new avenue to perform phase locking.

5. Sensitivity and Wavelength Sensing

We now demonstrate the application of our method to wavelength sensing.

Theory.—The maximum-magnitude FFT-pixel is taken for our spatial frequency reconstruction. Therefore, the main inaccuracies of the setup are the precision of the rotation angle $\Delta\theta$, the spatial frequency resolution determined by the precise image sensor dimensions, and a residual tilt of the image sensor.

The rotation angle resolution of the Newport M-URM80APP yields an expected wavelength sensing resolution of sub-pm/sub-fm for an angular rotation accuracy of $\Delta\theta = 0.1 \text{ deg}/0.001 \text{ deg}$, and we obtain the wavelength sensing resolution $\Delta\lambda_c$ (see Supporting Information S4 for details):

$$|\Delta\lambda_c| = \frac{\lambda^2 \Delta f_c}{2 \sin \psi + \lambda \Delta f_c}, \quad (9)$$

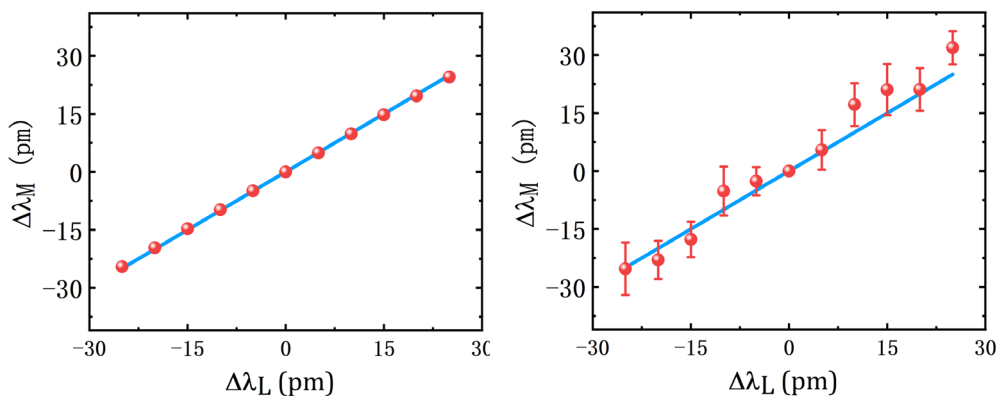


Figure 6. Demonstration of the high precision of wavelength sensing using our technique. The measured wavelength shift is indicated by red spheres for the numerical simulation (left) and experimental data (right). The blue line is the theoretical prediction results. The error bars represent the standard deviations corresponding to 15 independent measurements.

where Δf_c is the spatial frequency resolution and is determined by the image size L via $1/L$. The finite size of the image sensor yields an error of 60 pm. The latter clearly appears to be the more important limit on resolution for our demonstration experiment. We can improve this by spatial interpolation via zero-padding, which enables a significant increase in the resolution of the measured spatial frequencies. In our scheme, a zero-padding of up to $2^{18} \times 2^{10}$ pixels are performed for all results. To ensure a good SNR, the interference size is relevant since it straightforwardly influences the width of the Fourier spots and thus, the accuracy of the measured spatial frequencies.

Measurements. Experimentally, an external-cavity semiconductor laser at ≈ 776.3 nm (New Focus model 6224) with a linewidth of less than 300 kHz is coupled into our setup via a single-mode fiber. We scan the wavelength and measure it using a Fizeau-interferometer-based wavemeter (HighFinesse WS6-200).

Figure 6 shows our experimental results demonstrating ultrahigh wavelength resolution. Due to the stability of the tunable laser source and the absolute accuracy of the wavemeter (200 MHz) the wavelength was scanned in steps of 5 pm. The observed linear relation is in good agreement with theoretical analysis and numerical simulation, thereby confirming the wavelength shifts down to at least 5 pm or 2.5 GHz in frequency are readily discernable by our method. This accuracy can easily be improved by enlarging the interference pattern region, increasing intensity, using peak fitting for the determination of the spatial frequencies of the Fourier aliases, and fitting our model to the experimental data for many rotated pictures simultaneously.

Spectral performance. We can derive the spectral resolving power R that is equal to the ratio between the size of the zero-padded image and the interference period (See Supporting Information S5). The simplicity of the inverse relationship between the pixel size and the half length of the first Brillouin zone $\delta = 1/f_s$ means that, once the aliasing order is established, a unique mapping of spatial frequencies to wavelength is possible, without the need for postprocessing. For $\delta = 5.3$ μm pixel size, this is equivalent to a free spectral range (FSR) of $\Delta\nu = 20$ THz, much larger than the FSR of our Fizeau interferometers (WS6-200, 100 GHz) and standard Fabry–Perot cavities (several GHz). Our calculations in Equation (12) already resulted in a predicted wavelength

accuracy below a femtometer, thus a spectral resolving power beyond 10^8 , bringing it to the required sensitivity for probing the Doppler wobbles induced by exoplanets^[18] or the Zeeman-splitting of spectral lines of hydrogen and antihydrogen.^[19] However, a direct proof of this theoretically achievable accuracy would require an ultrastable, high-SNR system.

From our simple setup, it is evident that our technique could have several major advantages over the existing wavelength sensing techniques: higher resolution and experimental simplicity. Perhaps more importantly, systems containing optical elements such as lenses, gratings, or glass blocks (Fizeau interferometers) cannot be used for high-energy photons where media are strongly absorbing. Our technique is therefore suited for the extreme-ultraviolet (EUV) and x-ray regime where recent ptychographic methods have been explored^[20,21] with the added benefit of experimental simplicity.

6. Discussion and Outlook

We have shown that a simple arrayed image sensor in combination with Fourier analysis allows for deep-subpixel sensing of periodic interference patterns. This is possible by exploiting aliasing, and the absolute spatial frequencies as well as phase spectrum can be obtained by rotation of the sensor, even if it is square.

In a proof-of-principle experiment, we have demonstrated wavelength sensing with picometer resolution, potentially much simpler than Fizeau- or Fabry-Perot-based interferometers. Our method can also quite easily be applied to all wavelength ranges where arrayed image detectors are available, for instance, to metrology challenges in EUV lithography.

Our approach is quite general, it can be applied to other wave systems in nature, ranging from electromagnetic and acoustic waves to matter waves. We emphasize that the remarkable accuracy can be further improved by enlarging the interference region, using the fringe-lock,^[4] and improvements on rotational accuracy.

A promising extension and initial motivation of the study is applying our methods to the observation and characterization of bright superchiral fields.^[2] Additionally, combining our technique with concepts from quantum metrology could be

interesting: For instance, in the case that interfering light fields are not coherent states of light but $N00N$ states, an N -fold-enhanced resolution as compared with a classical interference lithography is possible,^[22–24] using an image sensor sensitive to multiphoton absorption or with single photon resolution. This is reminiscent of recent schemes with pixel super-resolution quantum imaging, which have been achieved by measuring the joint probability distribution of the spatial resolution of spatially entangled photons.^[25] Light fields with high-spatial frequency features appear also in other fields, such as by surface plasmon interference for nanolithography, at the interface between metals and dielectrics the wavelength of surface plasma waves can be down to the nanometer scale, while their frequencies remain in the optical range, going beyond the free-space diffraction limit of the light.^[26–28]

Supporting Information

Supporting Information is available from the Wiley Online Library or from the author.

Acknowledgements

The authors would like to thank Xinrui Wei, Jörg Götte, Koen van Kruining, and Robert Cameron for fruitful discussions and Michel Orrit for providing the wavemeter. This research was supported by EU H2020 (QLUSTER, 862035) from NWO (QUAKE, 680.92.18.04), from NWO/OCW (Quantum Software Consortium), from the National Natural Science Foundation of China (NSFC) (11874321 and 12174338), and from the Fundamental Research Funds for the Central Universities (2018FZA3005). Correction added on October 13th, 2023 after first online publication: Various typesetting errors were corrected.

Conflict of Interest

LW and WL filed a USPTO patent application “Image sensor-based interference fringe metrology with superresolution for laser beam angle and absolute frequency measurement” (number US 63/411252), which covers the concept and implementation described here.

Data Availability Statement

The data that support the findings of this study are available from the corresponding author upon reasonable request.

Keywords

Aliasing, frequency metrology, fringe metrology, optical interference, sub-sampling

Received: December 19, 2022

Revised: May 31, 2023

Published online: July 19, 2023

- [1] N. Gisbert Quilis, M. Lequeux, P. Venugopalan, I. Khan, W. Knoll, S. Boujday, M. Lamy De La Chapelle, J. Dostalek, *Nanoscale* **2018**, *10*, 10268.
- [2] K. C. van Kruining, R. P. Cameron, J. B. Götte, *Optica* **2018**, *5*, 1091.
- [3] D. Kouznetsov, Q. Deng, P. Van Dorpe, N. Verellen, *Phys. Rev. Lett.* **2020**, *125*, 184101.
- [4] C. G. Chen, P. T. Konkola, R. K. Heilmann, G. S. Pati, M. L. Schattenburg, *J. Vac. Sci. Technol. B Microelectron. Nanometer Struct.–Process., Meas., Phenom.* **2001**, *19*, 2335.
- [5] C. Joo, G. S. Pati, C. G. Chen, P. T. Konkola, R. K. Heilmann, M. L. Schattenburg, A. Liddle, E. H. Anderson, *J. Vac. Sci. Technol. B Microelectron. Nanometer Struct.–Process., Meas., Phenom.* **2002**, *20*, 3075.
- [6] S. Jiang, B. Lü, Y. Song, Z. Liu, W. Wang, L. Shuo, Bayanheshig, *Appl. Opt.* **2020**, *59*, 5830.
- [7] T. Chen, P. B. Catrysse, A. El Gamal, B. A. Wandell, in *Sensors and Camera Systems For Scientific, Industrial, Digital, And Photography Application*, SPIE, Bellingham, Washington USA **2000**, p. 451.
- [8] S. H. N. Alan Oppenheim, A. Willsky, *Signals and Systems*, Prentice Hall, New York, **1996**.
- [9] D. G. Voelz, *Computational Fourier Optics: A MATLAB Tutorial*, SPIE Press, Bellingham **2010**.
- [10] T. Bauer, S. Orlov, U. Peschel, P. Banzer, G. Leuchs, *Nat. Photonics* **2014**, *8*, 23.
- [11] D. Denkova, N. Verellen, A. V. Silhanek, V. K. Valev, P. Van Dorpe, V. V. Moshchalkov, *ACS Nano* **2013**, *7*, 3168.
- [12] N. Caselli, F. La China, W. Bao, F. Riboli, A. Gerardino, L. Li, E. H. Linfield, F. Pagliano, A. Fiore, P. J. Schuck, S. Cabrini, A. Weber-Bargioni, M. Gurioli, F. Intonti, *Sci. Rep.* **2015**, *5*, 9606.
- [13] T. Grosjean, I. A. Ibrahim, M. A. Suarez, G. W. Burr, M. Mivelle, D. Charraut, *Opt. Express* **2010**, *18*, 5809.
- [14] E. Schwartz, E. N. Ribak, *Appl. Opt.* **2017**, *56*, 1977.
- [15] P. de Groot, L. Deck, *Opt. Lett.* **1993**, *18*, 1462.
- [16] W. Luo, Y. Zhang, A. Feizi, Z. Göröcs, A. Ozcan, *Light Sci. Appl.* **2016**, *5*, e16060.
- [17] U. Sinha, C. Coureau, T. Jennewein, R. Laflamme, G. Weihs, *Science* **2010**, *329*, 418.
- [18] A. D. Sappey, P. Masterson, B. A. Sappey, *J. Opt. Soc. Am. B* **2020**, *37*, 3829.
- [19] A. Collaboration, *Nature* **2020**, *578*, 375.
- [20] M. Holler, M. Guizar-Sicairos, E. H. R. Tsai, R. Dinapoli, E. Müller, O. Bunk, J. Raabe, G. Aeppli, *Nature* **2017**, *543*, 402.
- [21] B. Zhang, D. F. Gardner, M. D. Seaberg, E. R. Shanblatt, H. C. Kapteyn, M. M. Murnane, D. E. Adams, *Ultramicroscopy* **2015**, *158*, 98.
- [22] H. Shin, K. W. C. Chan, H. J. Chang, R. W. Boyd, *Phys. Rev. Lett.* **2011**, *107*, 083603.
- [23] E. Toninelli, P.-A. Moreau, T. Gregory, A. Mihalyi, M. Edgar, N. Radwell, M. Padgett, *Optica* **2019**, *6*, 347.
- [24] Y. Kawabe, H. Fujiwara, R. Okamoto, K. Sasaki, S. Takeuchi, *Opt. Express* **2007**, *15*, 14244.
- [25] H. Defienne, P. Cameron, B. Ndagano, A. Lyons, M. Reichert, J. Zhao, A. R. Harvey, E. Charbon, J. W. Fleischer, D. Faccio, *Nat. Commun.* **2022**, *13*, 3566.
- [26] P. Dvořák, T. Neuman, L. Břínek, T. Šamořil, R. Kalousek, P. Dub, P. Varga, T. Šikola, *Nano Lett.* **2013**, *13*, 2558.
- [27] Z. W. Liu, Q. H. Wei, X. Zhang, *Nano Lett.* **2005**, *5*, 957.
- [28] W. Srituravanich, N. Fang, C. Sun, Q. Luo, X. Zhang, *Nano Lett.* **2004**, *4*, 1085.